Minimizing Measurement-Induced Errors in Viscoelastic MR Elastography

Samuel Kurtz, Bertrand Wattrisse, Elijah van Houten

Minimizing Measurement-Induced Errors in Viscoelastic MR Elastography

Samuel Kurtz, Bertrand Wattrisse, and Elijah E. W. Van Houten

***Abstract*— The inverse problem that underlies Magnetic Resonance Elastography (MRE) is sensitive to the measurement data and the quality of the results of this tissue elasticity imaging process can be influenced both directly and indirectly by measurement noise. In this work, we apply a coupled adjoint field formulation of the viscoelastic constitutive parameter identification problem, where the indirect influence of noise through applied boundary conditions is avoided. A well-posed formulation of the coupled field problem is obtained through conditions applied to the adjoint field, relieving the computed displacement field from kinematic errors on the boundary. The theoretical framework for this formulation via a nearly incompressible, parallel subdomain-decomposition approach is presented, along with verification and a detailed exploration of the performance of the methods via a numerical simulation study. In addition, the advantages of this novel approach are demonstrated *in-vivo* in the human brain, showing the ability of the method to obtain viable tissue property maps in difficult configurations, enhancing the accuracy of the method.**

***Index Terms*— Boundary conditions, inverse problems, magnetic resonance elastography (MRE), reconstructive imaging.**

I. Introduction

SOFT tissue viscoelastic properties are efficient biomarkers for clinical diagnosis [1], classification [2] or therapeutic monitoring [3]. Estimations of *in-vivo* constitutive parameters within a region of interest can be obtained using Magnetic Resonance Elastography (MRE) [4]. Over the past two decades, this non-invasive technique has been applied to a wide range of tissues [5], [6], [7] using different sources of excitation [8], [9] and investigating various mechanical properties [10], [11], [12]. A major advantage of MRE is its ability to provide quantitative material property estimates via different reconstruction processes, typically classified in two categories: direct and iterative methods [13]. Direct methods solve a linear minimization problem relying on the measured wave field to estimate material properties such as shear modulus [14], [15], [16]. The linear relation between the desired constitutive parameters and the deformation components of the governing equations guarantees uniqueness of the solution and fast computation. Variational formulations using virtual fields [17] have been developed to reduce dependence on noise [18]. However the differentiation of the motion data makes these methods dependent on the measurement quality and the associated data regularization methods.

Iterative methods, often referred to as nonlinear inversion (NLI), aim to provide a computed displacement field respecting the mechanical governing equations that replicates the noisy measured motion and allows the solution of a constrained minimization problem commonly represented by a least-squares objective function. The NLI method follows from a Lagrangian partial differential equation (PDE) used to derive a difference-driven forward problem comparing measured and computed displacement fields. One prominent NLI algorithm is a 3D parallel subdivision finite element scheme, called the *subzone* approach, based on a division of the global imaging problem into small, overlapping subdomains leading to local and global convergence and significantly reducing computation time [19]. In NLI methods, a reconstruction iteration firstly solves the forward problem (FP) for a given set of constitutive parameters to calculate the associated displacement field, and pressure field, for certain formulations. The algorithm then updates the material properties based on the gradient of the objective function. Numerous constitutive models supported by this algorithm have been developed, including linear elastic [20], viscoelastic [21] and poroelastic [22] formulations. Anisotropy has also been recently investigated for fibrous structures [23], [24]. Gradient computation was originally done with the Gauss-Newton method and has been extended to conjugate gradient and quasi-Newton methods [25]. Inversion stability is supported by the subzone overlap, which acts as a spatial filter [26], and total variation minimization [27] can also be applied.

Gradient calculation is performed efficiently using the adjoint equations of the forward problem for material property updates [28]. For linear viscoelastic models, the representative discretized FP is self-adjoint, thus requiring a single matrix inversion to compute both the calculated and adjoint displacement fields, considerably reducing computation time.

Samuel Kurtz is with Laboratoire de Mécanique et Génie Civil, CNRS, Université de Montpellier, 34090 Montpellier, France, and also with the Department of Mechanical Engineering, Université de Sherbrooke, Sherbrooke, QC J1K 2R1, Canada (e-mail: samuel.kurtz@umontpellier.fr).

Bertrand Wattrisse is with Laboratoire de Mécanique et Génie Civil, CNRS, Université de Montpellier, 34090 Montpellier, France (e-mail: bertrand.wattrisse@umontpellier.fr).

Elijah E. W. Van Houten is with the Department of Mechanical Engineering, Université de Sherbrooke, Sherbrooke, QC J1K 2R1, Canada (e-mail: elijah.van.houten@usherbrooke.ca).

A generalized adjoint method has been applied to NLI by Tan et al. for various mechanical models and gradient-based methods [29]. "Equilibrium-driven" and "difference-driven" equations developed in this adjoint model lead to a single, self-adjoint matrix, made invertible by the application of Dirichlet type boundary conditions, and referred to as the Displacement Field Condition (DFC) in this work, to solve the FP.

In the subzone NLI formulation, the kinematic field in the MRE PDE is driven by boundary conditions (BCs) obtained everywhere on the subzone boundary from the available displacement measurements. Assuming no significant internal pressure sources at the frequency of the applied tissue vibration, the Dirichlet BCs provide a suitable set of data for a well-posed solution to the FP. However, measured error introduced through these BCs may violate equilibrium due to their experimental nature, and additional regularization terms are required to stabilize the results of the mechanical property reconstruction process. In MRE, noise is often considered to be Gaussian based on its Magnetic Resonance Imaging (MRI) origins [30], and it is regularized by smoothing techniques. A recent study characterizing MRE-specific noise found image, physiological and vibration sources and concluded that their correlated nature increases error in NLI reconstructions [31]. The impact of displacement uncertainties in NLI-type gradient-based methods is almost entirely due to their indirect influence via the BCs of the FP, rather than their direct influence via the minimized objective function [32].

The goal of the method presented in this paper is to reduce the sensitivity to noisy BCs in the NLI-MRE problem. Inversion techniques that do not require BCs for the FP have been developed with promising results on numerical and phantom data. The Coupled Adjoint-State Equation describes a BC-free inverse elasticity problem based on the adjoint computation of the gradient by coupling solution of the displacement and adjoint field problems, leading to a system where the necessary BCs are applied uniquely to the adjoint field, a formulation referred to as the Adjoint Field Condition (AFC) in this work [33]. Moreover the Modified Error in Constitutive Equation approach introduces a "dynamically admissible" stress field as an independent variable in its functional to describe the discrepancy with the "kinematically admissible" strain field [34]. This method has been applied to viscoelasticity [35] as well as elastodynamics [36]. In this context, a direct material updating approach replaces gradient-based method by an analytical formulation of the constitutive parameters from the calculated stress and strain fields [37].

In this work, we develop and implement a novel formulation of the subzone NLI-MRE formulation for nearly incompressible viscoelastic materials based on previously demonstrated coupled approaches for the DFC and AFC. We apply this novel formulation to quantitative NLI-MRE analysis and investigate the efficiency of this approach with specific applications to simulated and *in-vivo* data.

Section II describes the mathematical framework developed to formulate the coupled Adjoint Field Condition (AFC), where BCs are uniquely applied to the adjoint field. The details of a MRE-inspired simulation study used for the validation of the method are also presented. Section III quantifies AFC vs DFC comparisons. Firstly, numerical results are focused on three important parameters for NLI-MRE reconstruction: noise, spatial resolution and initial guess. Afterwards, *in-vivo* brain reconstructions are presented to apply the method to real experimental data. Finally, the computational costs of the method are analyzed.

II. Methods

A. Forward Problem

1) Strong Form of the Forward Problem: The time-harmonic equilibrium equation for the complex displacement field, $\vec{u}$, in a domain Ω is given as

$$\vec{\nabla} \cdot \underline{\underline{\sigma}} = -\omega^2 \rho \vec{u} \qquad \text{in } \Omega \tag{1}$$

where $\underline{\underline{\sigma}}$ is the Cauchy stress tensor over Ω; ρ is the density and ω is the actuation frequency. Considering soft tissue as a linear viscoelastic and nearly incompressible continuum and ignoring the effects of anisotropy [38] and pre-stress [39], a mixed displacement-pressure formulation is used [29].

$$\begin{cases} \vec{\nabla} \cdot (G(\underline{\underline{\nabla}}\vec{u} + \underline{\underline{\nabla}}^T \vec{u}) - p\underline{\underline{\mathbb{I}}}) & = -\omega^2 \rho \vec{u} \quad \text{in } \Omega, \\ -\dfrac{p}{K} & = \vec{\nabla} \cdot \vec{u} \qquad \text{in } \Omega. \end{cases} \tag{2}$$

where G is the complex shear modulus; K is the complex bulk modulus; p is a pressure term; and $\underline{\underline{\mathbb{I}}}$ is the identity tensor. The material properties set can be described as $\theta = (G, K, \rho)$. The nearly incompressible condition leads to $K \gg G$ whereas $\vec{\nabla} \cdot \vec{u} \to 0$.

In general, direct formulations introduce the partition of the boundary, Γ, of the domain, Ω, into regions, Γ_D and Γ_N, respectively representing the portions of the surface described by known displacements or surface tractions. BCs are

$$\begin{aligned} \vec{u} &= \vec{u}_0 \text{ on } \Gamma_D, \\ \underline{\underline{\sigma}} \cdot \vec{n} &= \vec{t}_0 \text{ on } \Gamma_N, \end{aligned} \tag{3}$$

where $\vec{u}_0$ is the prescribed displacement on Γ_D while $\vec{t}_0$ is the traction acting on surface Γ_N, with a normal outward unit vector $\vec{n}$. Considering the lack of force measurement techniques for *in-vivo* situations, we will consider that $\Gamma_N = \emptyset$. The strong form of the FP described by (2) and (3) then requires measurements of the 3 displacement components on all the boundaries (*i.e.* $\Gamma = \Gamma_D$) in order to be well-posed. Measured displacements include experimental uncertainty, which can contradict the equilibrium conditions defined by (2). To avoid this contradiction, we introduce a specific formulation that does not depend on (3).

2) Weak Form of the Forward Problem: We introduce the space functions, $U(\theta) = (\vec{u}(\theta), p(\theta))^T$ and $W = (\vec{w}, q)^T$, to act as the trial and the test functions, respectively, used to develop the weak formulation of the FP [28]. Here, w are the test displacements, chosen to be zero on Γ, and q the test pressure. The goal is to calculate the displacement field $\vec{u}$ for a given set of material parameters θ. In the case where $\Gamma_N = \emptyset$, the FP weak form is given by the functional A, such that

$$A(W, U(\theta); \theta) = 0 \tag{4}$$

with

$$A(W, U(\theta); \theta) = \int_\Omega G(\underline{\underline{\nabla}}\vec{u} + \underline{\underline{\nabla}}^T\vec{u}) : \underline{\underline{\nabla}}\vec{w} - p\underline{\underline{\mathbb{I}}} : \underline{\underline{\nabla}}\vec{w} - \omega^2\rho\vec{u}\cdot\vec{w}\,d\Omega + \int_\Omega -(\vec{\nabla}\cdot\vec{u})q - \frac{pq}{K}\,d\Omega. \tag{5}$$

The viscoelastic FP defined in (5) is self-adjoint, meaning that $A(U(\theta), W; \theta) = A(W, U(\theta); \theta)$. This functional plays the role of a constraint in the MRE identification problem. The NLI quadratic objective function Φ is defined as the least-squares error between the calculated, material dependent, complex valued displacement field, $\vec{u}(\theta)$, and the measurement field, $\vec{u}_m$

$$\Phi(U(\theta)) = \frac{1}{2}\int_\Omega (\vec{u}(\theta) - \vec{u}_m)^H(\vec{u}(\theta) - \vec{u}_m)\,d\Omega, \tag{6}$$

where $x^H y$ is the hermitian product of x and y. The Lagrangian combining the least squares functional (6) and the constraint associated with the FP (5) is given by

$$L(W, U(\theta); \theta) = \Phi(U(\theta)) + A(W, U(\theta); \theta), \tag{7}$$

where W can be considered as a Lagrange multiplier in (7). Optimal conditions are computed from (7) by means of the directional derivatives, defined as the Gâteaux derivative $F'_x(\delta x) = \frac{d}{d\epsilon}F(x + \epsilon\delta x)|_{\epsilon=0}$, with respect to U, W and θ. The variation of L, L', is then given as

$$L' = L'_U(\delta U) + L'_W(\delta W) + L'_\theta(\delta\theta). \tag{8}$$

Considering variations δW and integrating $A(W, U(\theta); \theta)$ by parts, the optimal condition $L'_W(\delta W) = 0$ leads to the equilibrium-driven problem

$$\int_\Omega [-\vec{\nabla}\cdot G(\underline{\underline{\nabla}}\vec{u} + \underline{\underline{\nabla}}^T\vec{u}) + \vec{\nabla}p - \omega^2\rho\vec{u}]\cdot\delta\vec{w} - [(\vec{\nabla}\cdot\vec{u}) + \frac{p}{K}]\delta q\,d\Omega + \int_\Gamma [G(\underline{\underline{\nabla}}\vec{u} + \underline{\underline{\nabla}}^T\vec{u}) - p\underline{\underline{\mathbb{I}}}]\cdot\delta\vec{w}\cdot\vec{n}\,d\Gamma = 0. \tag{9}$$

Similarly, the optimal condition $L'_U(\delta U) = 0$ leads to the difference-driven problem

$$\int_\Omega [(\vec{u} - \vec{u}_m)^H - \vec{\nabla}\cdot[G(\underline{\underline{\nabla}}\vec{w} + \underline{\underline{\nabla}}^T\vec{w})] + \vec{\nabla}q - \omega^2\rho\vec{w}]\cdot\delta\vec{u} - [(\vec{\nabla}\cdot\vec{w}) + \frac{q}{K}]\delta p\,d\Omega + \int_\Gamma [G(\underline{\underline{\nabla}}\vec{w} + \underline{\underline{\nabla}}^T\vec{w})\cdot\delta\vec{u}]\cdot\vec{n}\,d\Gamma = 0. \tag{10}$$

Finally, the gradient for the inverse problem to determine the optimal material properties is obtained from the condition $L'_\theta(\delta\theta) = 0$, where, for w and u given by (10) and (9), respectively, such that $L'_U(\delta U) = L'_W(\delta W) = 0$, we have

$$L'_\theta(\delta\theta) = L' = \Phi'_\theta(U(\theta)) - A'_\theta(W, U; \delta\theta) = 0. \tag{11}$$

Here, as with most MRE cases, we will consider only reconstruction of the complex shear modulus, G, such that the gradient of the objective function, g_G, is given by

$$g_G = \Phi'_\theta(U(\theta)) = \int_\Omega (\underline{\underline{\nabla}}\vec{u} + \underline{\underline{\nabla}}^T\vec{u}) : \underline{\underline{\nabla}}\vec{w}\,d\Omega. \tag{12}$$

The following sections describe two different approaches for solving the adjoint FP defined by the equilibrium-driven problem (9) and difference-driven problem (10). The classical approach, previously detailed in [29] and referred to as the Displacement Field Condition (DFC), aims to perform a sequential resolution, using the displacement field $\vec{u}$ obtained by the equilibrium-driven problem to solve the difference-driven problem. A novel approach, referred to as the Adjoint Field Condition (AFC), aims to couple the solve of the two problems to remove the biased boundary conditions on the displacement field $\vec{u}$.

3) Displacement Field Condition: The DFC approach to the FP first solves the equilibrium-driven problem to calculate the trial functions $\vec{u}$ and p, denoted in the space $\mathcal{U}_\mathcal{D}$ such as

$$\mathcal{U}_\mathcal{D} = \{U = (\vec{u}, p) | \vec{u} \in H^1(\Omega), p \in H^1(\Omega), \vec{u} = \vec{u}_m \text{ on } \Gamma\}. \tag{13}$$

The problem associated to (9) and the Dirichlet condition in (3) is

$$\begin{cases} \vec{\nabla}\cdot(G(\underline{\underline{\nabla}}\vec{u} + \underline{\underline{\nabla}}^T\vec{u}) - p\underline{\underline{\mathbb{I}}}) + \omega^2\rho\vec{u} = 0 & \text{in } \Omega, \\ \vec{\nabla}\cdot\vec{u} + \dfrac{p}{K} = 0 & \text{in } \Omega, \\ \vec{u} = \vec{u}_m & \text{on } \Gamma. \end{cases} \tag{14}$$

The difference-driven problem aims to calculate the trial functions $\vec{w}$ and q, denoted in the space $\mathcal{W}_\mathcal{D}$ such as

$$\mathcal{W}_\mathcal{D} = \{W = (\vec{w}, q) | \vec{w} \in H^1(\Omega), q \in H^1(\Omega), \vec{w} = \vec{0} \text{ on } \Gamma\}. \tag{15}$$

Here, the calculated displacement $\vec{u}$ in (13) is used with (10) to calculate

$$\begin{cases} \vec{\nabla}\cdot(G(\underline{\underline{\nabla}}\vec{w} + \underline{\underline{\nabla}}^T\vec{w}) - q\underline{\underline{\mathbb{I}}}) + \omega^2\rho\vec{w} = \overline{\vec{u} - \vec{u}_m} & \text{in } \Omega, \\ \vec{\nabla}\cdot\vec{w} + \dfrac{q}{K} = 0 & \text{in } \Omega, \\ \vec{w} = \vec{0} & \text{on } \Gamma. \end{cases} \tag{16}$$

A detailed description of the discretized terms contained in (14), (16) and the corresponding gradient calculations is found in [29].

4) Adjoint Field Condition: The trial and test solution function spaces of the AFC approach, denoted respectively as $\mathcal{U}_\mathcal{A}$ and $\mathcal{W}_\mathcal{A}$ are

$$\mathcal{U}_\mathcal{A} = \{U = (\vec{u}, p) | \vec{u} \in H^1(\Omega), p \in H^1(\Omega)\},$$
$$\mathcal{W}_\mathcal{A} = \{W = (\vec{w}, q) | \vec{w} \in H^1(\Omega), q \in H^1(\Omega), \vec{w} = \vec{0} \text{ on } \Gamma\}. \tag{17}$$

The test function thus respects $\vec{w} = \vec{0}$ on Γ, such that the boundary terms in (9) and (10) can be ignored. While $\vec{u}$ and $\vec{w}$ are defined in a similar space, the system composed of (9) and (10) has no specified BCs on the displacement field, $\vec{u}$, contrary to the DFC approach in (14).

The Euler-Lagrange equations that define the coupled forward problem are obtained directly from (9) and (10), such

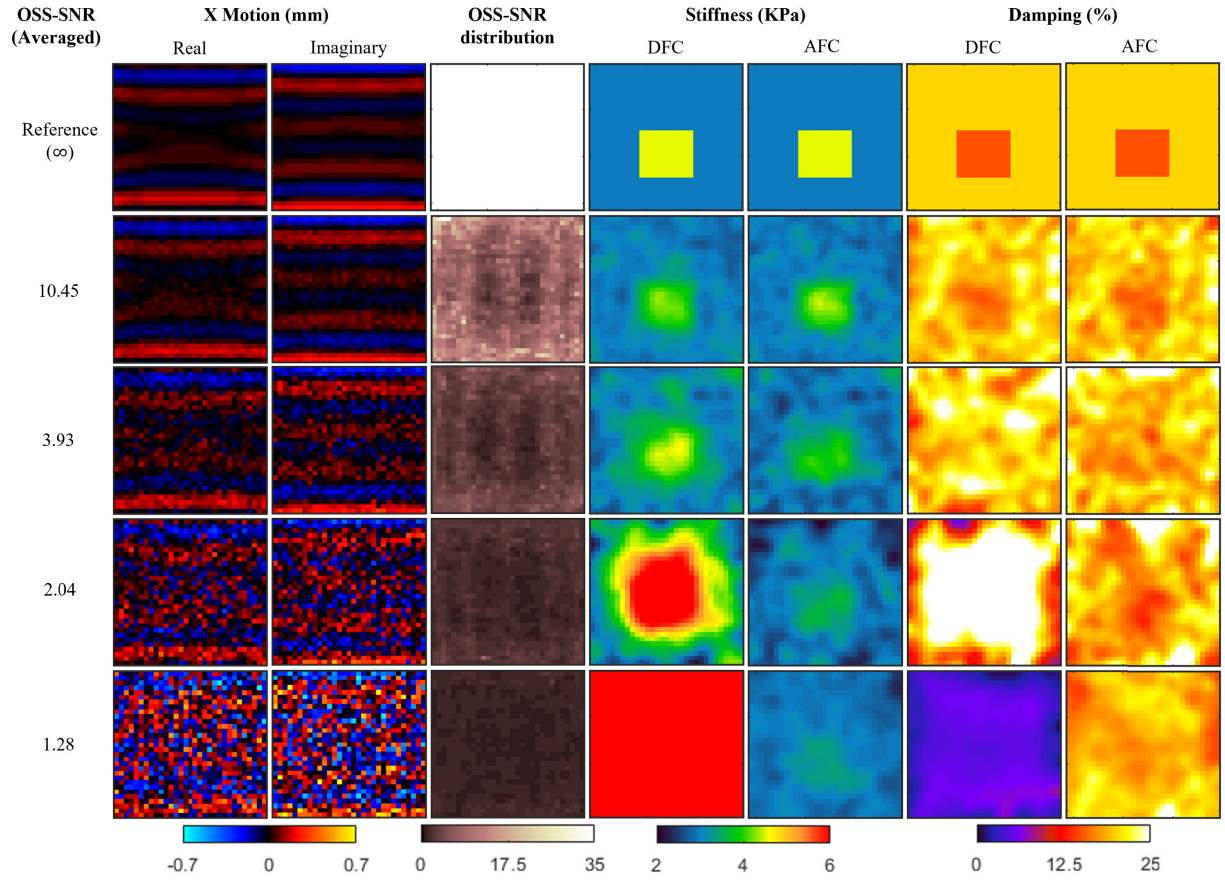

Fig. 1. A representative slice of the first displacement field components, distributed OSS-SNR, estimated shear stiffness and damping ratio using AFC and DFC formulations. Reference values and 4 levels of OSS-SNR are shown.

that

$$\begin{cases} \vec{u} - [\vec{\nabla} \cdot (G(\underline{\underline{\nabla}}\vec{w} + \underline{\underline{\nabla}}^T \vec{w}) - q\underline{\underline{\mathbb{I}}}) + \omega^2 \rho \vec{w}] = \vec{u}_m & \text{in } \Omega, \\ \vec{\nabla} \cdot \vec{w} + \dfrac{q}{K} = 0 & \text{in } \Omega, \\ \vec{\nabla} \cdot (G(\underline{\underline{\nabla}}\vec{u} + \underline{\underline{\nabla}}^T \vec{u}) - p\underline{\underline{\mathbb{I}}}) + \omega^2 \rho \vec{u} = 0 & \text{in } \Omega, \\ \vec{\nabla} \cdot \vec{u} + \dfrac{p}{K} = 0 & \text{in } \Omega, \\ \vec{w} = 0 & \text{on } \Gamma. \end{cases} \tag{18}$$

These coupled FP equations, referred to as the AFC, are implemented and solved via a finite element method model. One possible system representing this formulation is

$$[\mathbf{A}]\{\mathbf{x}\} = \{\mathbf{f}\}, \tag{19}$$

given by the Hermitian block matrix

$$[\mathbf{A}] = \begin{bmatrix} [\mathbf{I}] & [\mathbf{0}] & [\mathbf{K}]^H - \omega^2 [\mathbf{M}]^H & [\mathbf{A_p}]'^H \\ [\mathbf{0}] & [\mathbf{0}] & [\mathbf{A_p}]^H & [\mathbf{A_d}]^H \\ [\mathbf{K}] - \omega^2 [\mathbf{M}] & [\mathbf{A_p}]' & [\mathbf{0}] & [\mathbf{0}] \\ [\mathbf{A_p}] & [\mathbf{A_d}] & [\mathbf{0}] & [\mathbf{0}] \end{bmatrix}, \tag{20}$$

with $[\mathbf{K}]$ the stiffness matrix, $[\mathbf{M}]$ the mass matrix, $[\mathbf{A_p}]$ and $[\mathbf{A_d}]$ matrices related to pressure terms, and $[\mathbf{I}]$ the identity matrix. The solution vector is given as

$$\{\mathbf{x}\} = \begin{Bmatrix} \{\mathbf{U}\} \\ \{\mathbf{W}\} \end{Bmatrix} = \begin{Bmatrix} \{\mathbf{u}\} \\ \{\mathbf{p}\} \\ \{\mathbf{w}\} \\ \{\mathbf{q}\} \end{Bmatrix}, \tag{21}$$

and the right-hand-side vector is given as

$$\{\mathbf{f}\} = \begin{Bmatrix} \{\mathbf{u_m}\} \\ \{\mathbf{0}\} \\ \{\mathbf{0}\} \\ \{\mathbf{0}\} \end{Bmatrix}, \tag{22}$$

with $\{\mathbf{u}\}$ and $\{\mathbf{p}\}$ the main displacement and pressure discretized fields grouped by $\{\mathbf{U}\}$, $\{\mathbf{w}\}$ and $\{\mathbf{q}\}$ the adjoint displacement and pressure discretized fields grouped by $\{\mathbf{W}\}$, and $\{\mathbf{u_m}\}$ the measurement field.

The matrix factorization is performed by the MUMPS library [40]. Once $\{\mathbf{U}\}$ and $\{\mathbf{W}\}$ are obtained from the solution of (19), variations *w.r.t.* material properties leads to the discretized form of the gradient described by (12) [41]. A detailed description of the discretized terms contained in (18) and the corresponding gradient calculations is found in [29].

B. Simulation Study Description

A simulation study is developed to show the effectiveness of the subzone AFC formulation. Reconstructions are performed

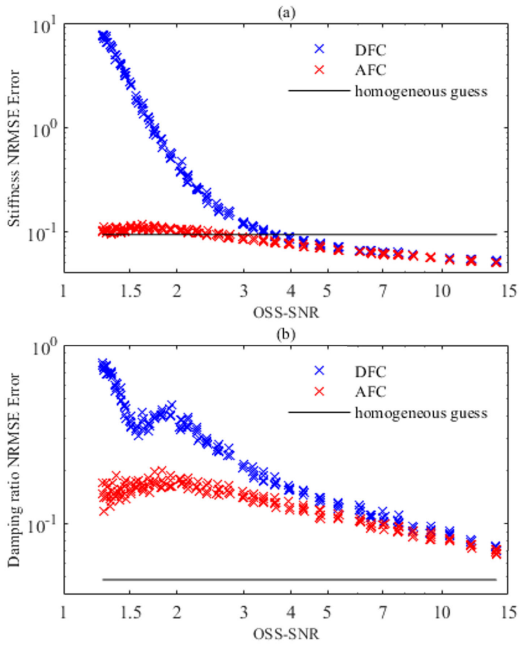

Fig. 2. NRMSE of the reconstructed shear stiffness (a) and damping ratio (b) using DFC (blue) and AFC (red) approaches for different averaged OSS-SNR. The homogeneous guess line is the NRMSE error considering a completely homogeneous reconstruction defined by a volume ratio of the inclusion and matrix parameter values. Note that the volume fraction of the inclusion only represents 3.7% of the reconstruction mesh nodes, explaining low values of homogeneous guess.

on a MRE inspired, full-field, 3D viscoelastic solid. We consider a 10 cm cubic block with a stiff 3 cm cubic inclusion off-centered by [0,1,-1] cm relative to the center of the surrounding block. In order to generate multi-directional shear waves within the domain, a prescribed tangential, uniaxial, harmonic displacement of 1 μm amplitude is applied to every face of the block at an actuation frequency of 70 Hz.

Both matrix and inclusion materials have homogeneous, isotropic, nearly incompressible viscoelastic properties defined by their complex shear modulus $G = G' + iG''$ and bulk modulus K. For the purpose of easier interpretation, we consider the following material properties

$$\mu = \frac{2|G|^2}{G' + |G|} \text{ and } \xi = \frac{G''}{2G'} \tag{23}$$

where μ is the real-valued dynamic shear stiffness associated with the time-harmonic shear wave, and ξ is the viscoelastic damping ratio. The target viscoelastic shear stiffness and damping ratio for the matrix material are respectively set to $\mu^{\mathrm{M}}_{\mathrm{ref}} = 3$ kPa; $\xi^{\mathrm{M}}_{\mathrm{ref}} = 20\%$, with the inclusion material properties set as $\mu^{\mathrm{I}}_{\mathrm{ref}} = 1.5\mu^{\mathrm{M}}_{\mathrm{ref}}$; $\xi^{\mathrm{I}}_{\mathrm{ref}} = 0.75\xi^{\mathrm{M}}_{\mathrm{ref}}$. Matrix and inclusion materials are nearly incompressible, with Poisson's ratio $\nu = 0.495$, and have a homogeneous mass density, $\rho = 1000$ kg.m^{-3}.

Complex numerical "measurements" are generated by a finite element simulation using COMSOL Multiphysics® (v. 4.1, COMSOL AB, Stockholm, Sweden). The time-harmonic formulation is implemented by a solid mechanics module stationary solver with an added inertial term $\rho\omega^2\vec{u}$. Material viscosity is introduced by complex valued modulus G. The target material parameters were (i) discretized by a quadratic tetrahedral (TET10) 10^5 element mesh; (ii) interpolated to a regular grid used to construct a coarser reconstruction mesh using 6720 quadratic hexahedral (HEX27) elements; and (iii) corrupted by a random noise. Consistent with experimental measurement data, real and imaginary components of the displacement must suffer perturbations coming from equivalent, yet uncorrelated distribution laws [42]. For the k^{th} component of the interpolated displacement $\tilde{u}_k = \tilde{u}'_k + i\tilde{u}''_k$, $\delta\tilde{u}'_k$ and $\delta\tilde{u}''_k$ are respectively the real and imaginary components of the perturbation. These perturbations allow the definition of the k^{th} component of the noisy interpolated displacement, $\hat{u}_k$, as

$$\hat{u}_k = \tilde{u}'_k + \delta\tilde{u}'_k + i(\tilde{u}''_k + \delta\tilde{u}''_k). \tag{24}$$

These perturbations are given as

$$\delta\tilde{u}'_k = \max(\tilde{u}')\frac{\mathrm{SNR_m}}{\sqrt{2}}r_k \text{ and } \delta\tilde{u}''_k = \max(\tilde{u}'')\frac{\mathrm{SNR_m}}{\sqrt{2}}q_k \tag{25}$$

where r_k and q_k are normal random variables with zero mean and unit variance; $\mathrm{SNR_m}$ is a signal-to-noise ratio based on the maximum value of the displacement field. In several MRE studies e.g., [11] and [23], the percentage of artificial SNR is based on mean displacement values, rather than maximum values, limiting direct comparison of noise levels with this work. For each dataset with added noise, the calculated metric to quantify the error is the octahedral shear strain-based SNR (OSS-SNR) [43], where

$$\text{OSS-SNR} = \frac{\overline{\mathrm{OSS}(\hat{u})}}{\overline{\mathrm{OSS}(\delta\tilde{u})}}. \tag{26}$$

Note that this definition is somewhat different from the OSS-SNR formulation used for *in-vivo* applications which is based on the upper harmonics of the Fast Fourier Transform, limiting direct comparison of OSS-SNR levels observed here (*in-silico*) and *in-vivo*. Noisy displacement datasets are converted to mechanical property maps using the DFC and AFC formulations of the subzone NLI algorithm. Material properties are reconstructed on a mesh based on the measurement, isotropic $2.94 \times 2.94 \times 2.94$ mm^3 grid. A 4.4 mm cubic 3D Gaussian filter was applied on the reconstructed properties [25]. The parallel computations are carried out on the *Beluga* and *Narval* computing clusters managed by *The Digital Research Alliance of Canada*. In this study, μ and ξ are updated iteratively via reconstruction of G' and G''. Initial constitutive parameters, referred to as the initial guess, are assumed homogeneous. The initial shear stiffness, μ_0, is varied in the following study, while the initial damping ratio is set as $\xi_0 = 0.9\xi^M_{REF}$.

The time-harmonic inverse problem quality is highly dependent on the wave description available in the identification domain. A key parameter in the NLI approach reconstruction is the size of the subzone [44], described in this work by the block material's mechanical wavelength to subzone size ratio λ^M/L_Z. A large subzone size, denoted by smaller values of λ^M/L_Z, generally increases the resolution of the shear wave, at the cost of increased computational time.

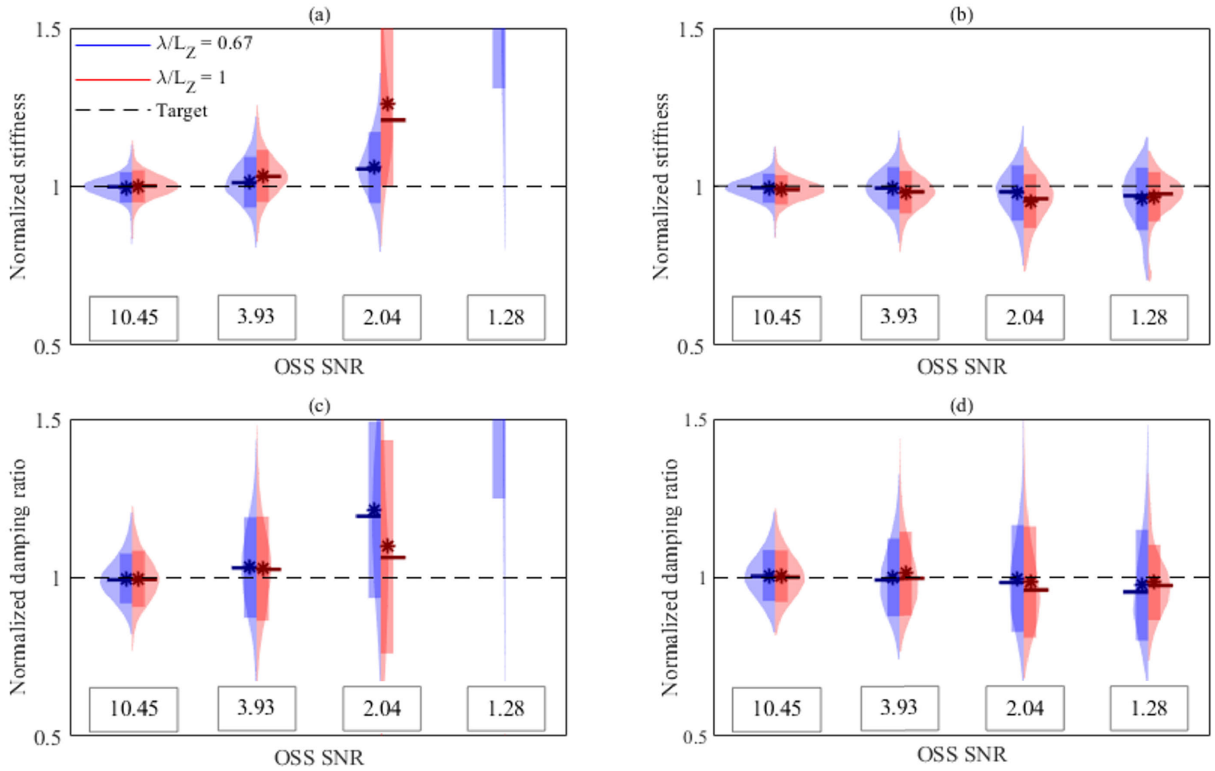

Fig. 3. Normalized reconstructed stiffness (a,b) and damping ratio (c,d) distributions over 4 OSS-SNR for 2 subzone sizes set using DFC (a,c) and AFC (b,d) formulations, including mean (star), median (rod), kernel density (light bell curve) and quartiles (dark box rectangle).

III. Verification

A. Simulation Study: Noise Sensitivity

For this study, we reconstruct 180 data instances, with OSS-SNR ranging from 1.28 to 14. Initial shear stiffness was set as $\mu_0/\mu^M_{REF} = 1$ and the subzone size was fixed by $\lambda^M/L_Z = 1$. Reconstructions using both AFC and DFC formulations were performed. Reconstruction quality is evaluated using the Normalized Root Mean Square Error, $\text{NRMSE}_X = \frac{||X-X_{REF}||}{||X_{REF}||}$, where X is the identified material property field, μ or ξ. Errors were plotted relative to OSS-SNR for each problem type (DFC or AFC).

Fig. 1 provides a qualitative overview of results from this identification test. For low levels of noise, estimated material properties are correctly recovered for both AFC and DFC. A high level of noise makes the wave-like nature of the displacement field difficult to visualize. The loss of this wavelength signal impacts the OSS-SNR and the quality of the material property reconstruction. In this situation, the DFC identification process over-estimates the shear stiffness and under-estimates the damping ratio, associating the noisy motion data to a rigid, nearly elastic medium. The AFC estimations remain accurate around a reasonable range of values for both properties. Locally stiff regions associated with the inclusion are detectable. Material properties identified by AFC over the represented slice have a larger variance at an OSS-SNR level of 2.04 than an OSS-SNR level of 1.28, illustrating this trend.

Fig. 2 demonstrates the quantitative sensitivity to noise of the mechanical properties identification. AFC and DFC have similar results for shear stiffness estimation at OSS-SNR levels greater than 7. However, below this level, DFC NRMSE rises exponentially with decreasing of OSS-SNR, due to over-estimation of stiffness and under-estimation of damping ratio, whereas AFC NRMSE increases roughly linearly with noise. For OSS-SNR levels lower than 2, NRMSE decreases slightly for the AFC formulation. This observation can be associated with the reduced variance in the identified properties at these low signal levels. As OSS-SNR levels of 3 and lower, stiffness identification accuracy of AFC stays close to the homogeneous guess associated with the block modulus.

B. Simulation Study: Effects of Reconstruction Parameters

The reconstruction problem is considered for 4 instances of OSS-SNR from 1.28 to 10.45, covering a range of data quality scenarios. Distribution profiles of the reference-normalized identified properties in the full domain represent the reconstruction accuracy and the associated impact of the varied reconstruction parameters. Reconstructed properties through the center of the inclusion along a line in the x-axis are also analyzed. First, the initial guess is set as $\mu_0/\mu^M_{REF} = 1$ and subzone size is varied, $\lambda^M/L_Z = [0.67; 1]$. Second, subzone sizes are set to $\lambda^M/L_Z = 1$, to investigate initial guess impact using two sets of initial shear stiffness: $\mu_0/\mu^M_{REF} = [0.7; 1.5]$.

Fig. 3 shows that property reconstruction results roughly follow a normal distribution. Subzone size has an impact on the DFC based identification process with noisy data. Estimated material properties profiles have Gaussian distributions and are similar for both AFC and DFC at high OSS-SNR

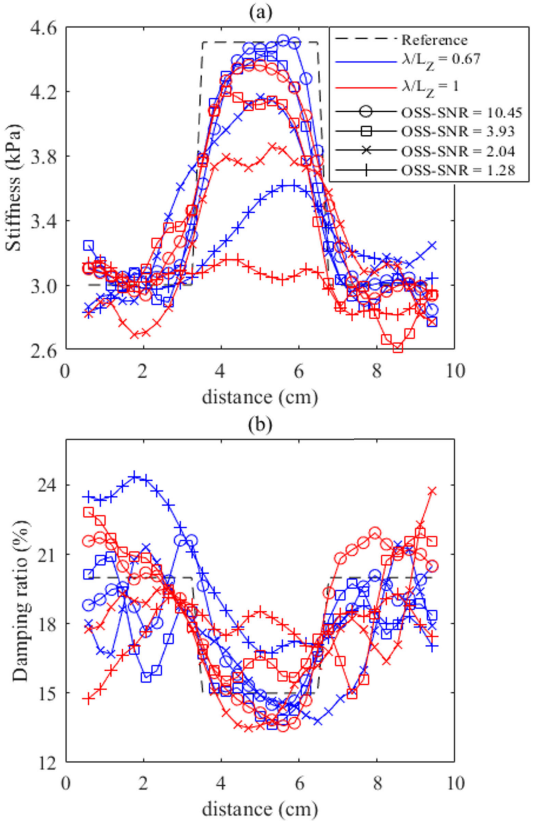

Fig. 4. A representative line plot of reconstructed stiffness (a) and damping (b) using AFC with 4 different level of input noise. Two spatial resolutions subzone sizes results are plotted (higher in blue, lower in red).

TABLE I
AVERAGE NORMALIZED RECONSTRUCTED PARAMETERS ON THE INCLUSION REGION FOR 2 SUBZONE SIZE SETS AND 4 OSS-SNR SETS USING AFC

OSS-SNR	λ^M/L_Z	$\overline{\mu^{\mathrm{I}}}/\mu^{\mathrm{I}}_{\mathrm{REF}}$	$\overline{\xi^{\mathrm{I}}}/\xi^{\mathrm{I}}_{\mathrm{REF}}$
10.45	1.0	0.88	1.10
10.45	0.67	0.90	1.09
3.93	1.0	0.85	1.11
3.93	0.67	0.88	1.09
2.04	1.0	0.78	1.02
2.04	0.67	0.84	1.12
1.28	1.0	0.72	1.19
1.28	0.67	0.75	1.16

levels. Lower signal leads to stiffer mean and higher variance in the DFC identified properties. DFC results at 2.04 OSS-SNR show that reconstructed properties are more scattered for a smaller subzone size, demonstrating that inaccuracy in the identification process is highly related to subzone resolution when BCs are involved.

The same level of noise using AFC provides correct mean values and distribution profiles, indicating a reduced global impact of subzone size for the AFC formulation. In order to evaluate the heterogeneity detection, Fig. 4 shows, along a representative line, the sensitivity of AFC identified properties to different levels of noise and subzone sizes. As expected, accuracy decreases as the noise increases. Reconstructed property values for larger subzones, $\lambda^M/L_Z = 0.67$, show

TABLE II
AVERAGE NORMALIZED RECONSTRUCTED PARAMETERS ON THE INCLUSION REGION FOR 2 INITIAL GUESS SETS AND 4 OSS-SNR SETS USING AFC

OSS-SNR	μ_0/μ^M_{REF}	$\overline{\mu^{\mathrm{I}}}/\mu^{\mathrm{I}}_{\mathrm{REF}}$	$\overline{\xi^{\mathrm{I}}}/\xi^{\mathrm{I}}_{\mathrm{REF}}$
10.45	0.7	0.88	1.10
10.45	1.5	0.88	1.10
3.93	0.7	0.85	1.11
3.93	1.5	0.85	1.10
2.04	0.7	0.78	1.02
2.04	1.5	0.78	1.02
1.28	0.7	0.71	1.12
1.28	1.5	0.83	1.37

slightly better accuracy than smaller subzones at each SNR level, with a more pronounced effect at higher noise levels. Focusing on the whole inclusion, Table I provides a quantitative evaluation of this observation. While identified parameters in this region using AFC are closer to the reference values for larger subzones, differences between the two subzones size reconstructions never exceed 10%.

Fig. 5 shows that both AFC and DFC identified material properties provide similar mean and distribution profiles for OSS-SNR levels above 3, regardless of the initial guess. For lower levels of OSS-SNR, DFC results start to diverge from AFC results significantly. For OSS-SNR of 1.28, the scatter profiles of AFC results are similar but the mean value of the over-estimated initial shear modulus is superior than the under-estimated one, illustrating the indeterminate nature of the inverse problem in this low signal condition. Table II shows that these global observations for AFC are identical in the inclusion region and thus that the initial guess has a minor impact on the heterogeneity detection.

C. In-Vivo Brain Study

Data from a healthy, young adult brain, used in a recent study from Smith et al. [24], are investigated via AFC and DFC NLI-MRE reconstructions. Considered data include a high SNR data set from an anterior-posterior (AP) excitation and a low SNR set from a left-right (LR) excitation. Visual and quantitative comparisons between reconstructed parameters are provided comparing AP and LR data and AFC and DFC based reconstruction. Retaining a similar subzone NLI parametrization as used in the original study, reconstructed material properties maps are recovered on an isotropic $2.0 \times 2.0 \times 2.0$ mm^3 grid, using both AFC and DFC formulations. Subzone are set on an isotropic $20 \times 20 \times 20$ mm^3 grid with a 15% overlap. Initial parameters are set as $\mu_0 = 3.3$ kPa, $\xi_0 = 18\%$, $K = 1.68$ MPa and $\rho = 1000$ kg.m^{-3}. A 3.0 mm large Gaussian filter was applied to the reconstructed properties. Variations in the results due to excitation (and thus SNR) are analyzed with absolute mean difference (MD) and NRMSE of the reconstructed AP and LR data.

Fig. 6 shows that the AFC formulation provides more precise MRE reconstruction results across different signal levels. The AP shear stiffness reconstructions using DFC and AFC are in good agreement. The DFC reconstruction of the

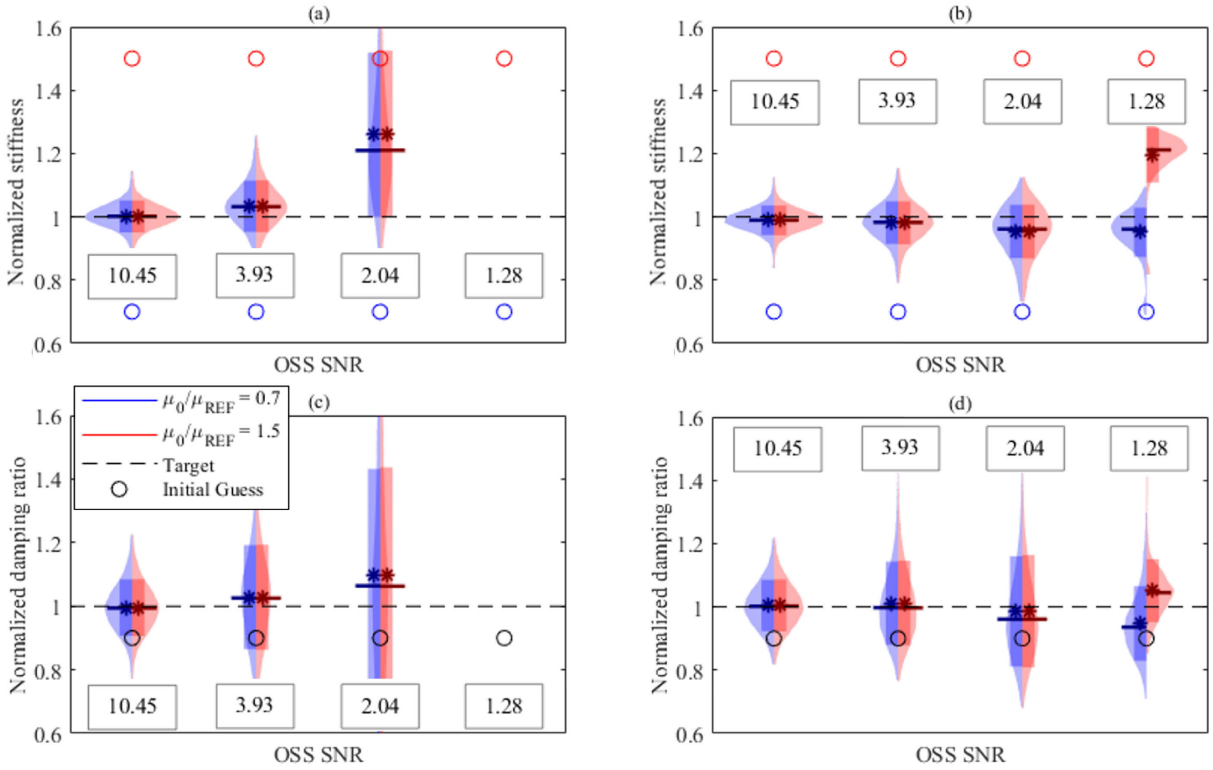

Fig. 5. Normalized reconstructed stiffness (a,b) and damping ratio (c,d) distributions over 4 OSS-SNR for 2 initial guess set using DFC (a,c) and AFC (b,d) formulations, including mean (star), median (rod), kernel density (light bell curve) and quartiles (dark box rectangle). The homogeneous initial values for under-estimated (blue dot) and over-estimated (red dot) shear stiffness as well as initial damping ratio (black dot) are indicated. DFC estimates for the OSS-SNR level of 1.28 are out of figure window in (a,c).

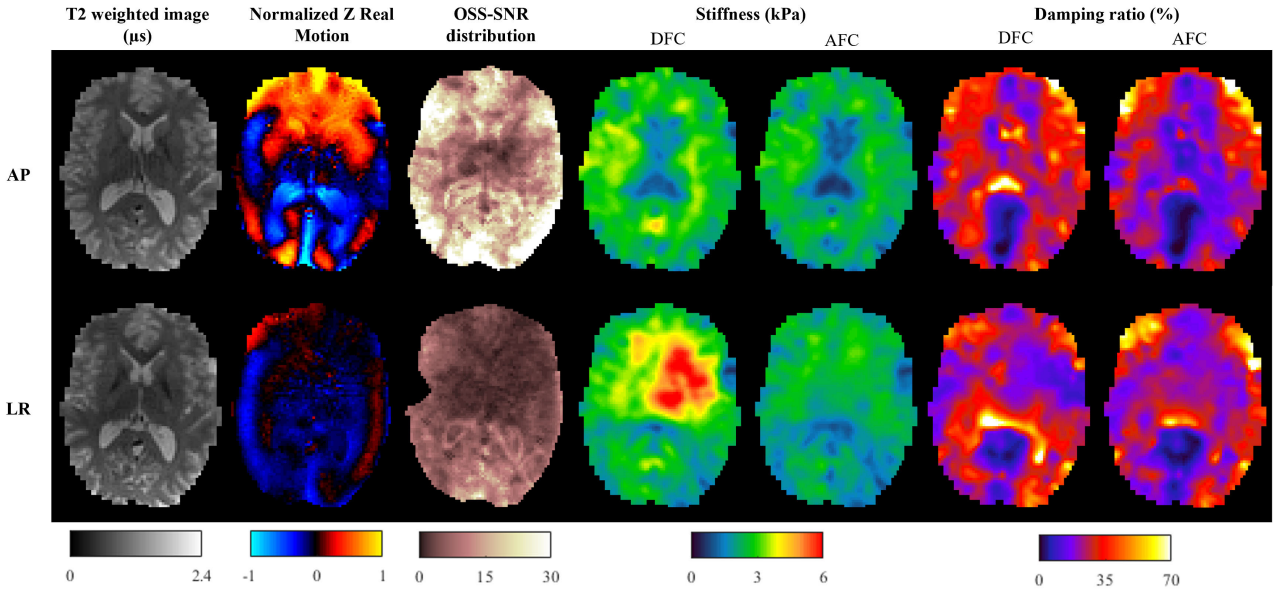

Fig. 6. A representative slice of the T2 weighted image, real part of the out of plane displacement field, distributed OSS-SNR, estimated shear stiffness and damping ratio using AFC and DFC formulations for the anterior-posterior (AP) and left-right (LR) data.

LR data suffers from an over-estimated, asymmetrical region related to a drop in SNR, while AFC reconstruction avoids this increase in shear stiffness in the affected region. Other regions with better local SNR show good similarities between LR reconstructions using DFC and AFC, as well as a good similarity between AP and LR datasets using AFC. Table III indicates that the mismatch for both stiffness and damping ratio reconstructions is reduced by roughly half with AFC based reconstructions.

D. Simulation Time

In the DFC formulation, two forward resolutions are required: the force-driven problem provides space function solutions that are used for the difference-driven problem.

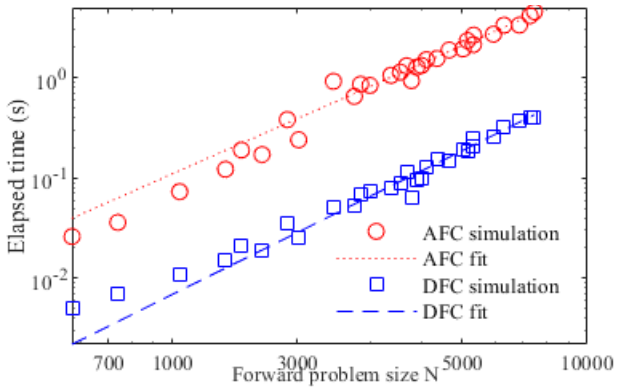

Fig. 7. Computational time of the forward problem defined by the number of unknowns for DFC and AFC formulations. The bandwidth-based power law regression is indicated.

TABLE III
AVERAGE DIFFERENCES BETWEEN AP AND LR RECONSTRUCTED PARAMETERS

	$\overline{\lvert\mu_{AP}-\mu_{LR}\rvert}$ (kPa)	$\overline{\lvert\xi_{AP}-\xi_{LR}\rvert}$ (%)
DFC	0.686	47.0
AFC	0.365	22.3

Although these problems are different, the underlying PDEs are self-adjoint (for viscoelastic materials), such that they share the same discretization matrix and only one LU factorization is required. Using a Gaussian substitution, computational cost is mainly driven by this factorization stage, estimated for a $n \times n$ matrix with a bandwidth of b_D to be $O(b_D^2 n)$ [45]. Because of the displacement-pressure formulation of the incompressibility condition, average bandwidth is difficult to predict and here is set to respect $b_D = n^{\alpha_D}$ with $\alpha_D \in [0, 1]$. The novel AFC formulation includes both space and test functions, thus matrix size is doubled and computation cost is estimated to be $O(2b_A^2 n)$, with the bandwidth $b_A = (2n)^{\alpha_A}$ again determined by $\alpha_A \in [0, 1]$.

In this simulation study, the forward problem size is related to the number of unknown degrees of freedom, u and p, defined as N, which is loosely controlled by the subzone size. Forward problem sizes ranging from $N = 500$ to $N = 7500$ are studied and computation times for both DFC and AFC approaches are fitted by a power law. Fig. 7 shows that computational time correctly fits with the number of unknowns for both approaches ($R^2 > 0.98$). Computational time of the AFC formulation is roughly 10 times longer than the DFC. Average bandwidth determined by regression of AFC and DFC results scales to $\alpha_A = 0.41$ and $\alpha_D = 0.53$, respectively. The difference in computational time decreases with the size of problem given that $\alpha_D > \alpha_A$, *i.e.* the AFC matrix is sparser than the DFC matrix.

IV. DISCUSSION

Simulation and *in-vivo* applications show that the coupled, BC-free formulation of the FP provides a significant improvement of the subzone NLI algorithm, considering typical *in-vivo* MRE conditions.

We demonstrate that avoiding the indirect introduction of measurement noise through BCs into the NLI-MRE reconstruction process improves the accuracy of the reconstructed viscoelastic material properties in low SNR cases. This result offers a new SNR threshold for MRE treated by the subzone NLI method, and other related methods. Previous studies using the generalized adjoint formulation of this algorithm were based on a strain-based signal-to-noise ratio equal to 3 [46]. In this study, reconstructions error using this novel AFC formulation was lower than error based on the previous DFC formulation at this threshold, indicating that it could be removed, although the sensitivity to heterogeneities is still related to the SNR level.

The question of subzone size was investigated by comparing results with varying ratios of mechanical wavelength and subzone size. In agreement with previous studies of this parameter [44], our analysis recovers the "zone size effect" previously observed in the identified material moduli under high noise levels, when using the previous BC-based approach (DFC) and shows how the novel BC-free formulation (AFC) provides accurate results, regardless of noise level, for a subzone size equal to the mechanical wavelength. Considering that zone size plays an important role in the subdomain based inverse problem due to computational time and memory limitations, this novel formulation offers a robust and stable approach to the subzone based NLI algorithm.

All the simulation results based on AFC demonstrate a sensitivity to material heterogeneity, although the accuracy of the stiffness and damping characterization remains related to SNR. This result demonstrates the effectiveness of the novel formulation for repeatable assessment of material properties even in varying levels of SNR.

We also investigate effects of initial guess for the reconstruction processes. Overall error due to initial shear stiffness was reduced by the AFC based reconstruction process, showing that AFC remains sensitive to signal, regardless of the noise level. We observed that error in the model induced by a bad initial guess only impacts the mean value of the reconstructed properties, while the variance in the final solution is less affected. This result is associated with a change in convexity of the error functional around the expected minimum at high noise levels. Identification results starting from opposing initial guesses could provide broader characterization of the property estimate and its variance.

Preliminary *in-vivo* brain reconstructions confirm the simulation results. The novel formulation recovers similar values and variance in reasonable SNR regions while reducing the problematic over-estimation of the shear stiffness caused by the drop of signal in the DFC formulation. The mismatch between reconstructions from two different excitations (AP and LR) was significantly reduced with the AFC formulation. Considering that the anisotropy of such structures leads to less than 20% of difference between AP and LR reconstructions [38], this result demonstrates excellent reproducibility for real MRE data. This outcome makes possible the use of NLI for low SNR situations such as pre-clinical MRE studies [47]. Further works could consider the detection of smaller heterogeneities by decreasing the regularization parametrization in accordance to this increased stability.

Finally, solving for both the displacement and adjoint fields in a single operation increases the computational time of the

forward problem while other operations of the NLI algorithm such as gradient computation or the subzone filtering remain unchanged. Based on numerical results previously presented, a practical approach to reduce this constraint while ensuring decent reconstructions would be to compute using smaller subzones.

V. Conclusion

An efficient algorithm of the adjoint-based forward problem for the nearly incompressible viscoelastic MRE inversion problem is presented. The force-driven and the difference-driven problems are formulated by a unique discrete operation where boundary terms are no longer required in the force-driven problem. Thus, the equilibrium PDE is satisfied without the use of experimental measurements that may violate the kinematic admissibility condition. Simulation and *in-vivo* brain reconstructions examples confirm that this novel formulation broadly enhances the performance of the subzone based NLI-MRE problem in low SNR cases and reduces the dependence on the initial guess and problem size in these cases. This approach is readily extensible to more suitable tissue mechanics models such as those used for anisotropic fibrous tissues [23].

Acknowledgment

The authors would thank to thank Prof. Curtis L. Johnson and Daniel R. Smith from the Mechanical Neuroimaging Laboratory, University of Delaware, for providing the *in-vivo* data used in Section III-C.

References

[1] G. Rus, I. H. Faris, J. Torres, A. Callejas, and J. Melchor, "Why are viscosity and nonlinearity bound to make an impact in clinical elastographic diagnosis?" *Sensors*, vol. 20, no. 8, p. 2379, Apr. 2020. [Online]. Available: https://www.mdpi.com/1424-8220/20/8/2379

[2] L. V. Hiscox et al., "Standard-space atlas of the viscoelastic properties of the human brain," *Human Brain Mapping*, vol. 41, no. 18, pp. 5282–5300, Dec. 2020. [Online]. Available: https://onlinelibrary.wiley.com/doi/10.1002/hbm.25192

[3] A. Bohte et al., "Breast magnetic resonance elastography: A review of clinical work and future perspectives," *NMR Biomed.*, vol. 31, no. 10, Oct. 2018, Art. no. e3932. [Online]. Available: https://onlinelibrary.wiley.com/doi/10.1002/nbm.3932

[4] I. Sack, "Magnetic resonance elastography from fundamental soft-tissue mechanics to diagnostic imaging," *Nature Rev. Phys.*, vol. 5, no. 1, pp. 25–42, Nov. 2022, doi: 10.1038/s42254-022-00543-2.

[5] S. Singh et al., "Diagnostic performance of magnetic resonance elastography in staging liver fibrosis: A systematic review and meta-analysis of individual participant data," *Clin. Gastroenterol. Hepatol.*, vol. 13, no. 3, pp. 440–451, Mar. 2015. [Online]. Available: https://linkinghub.elsevier.com/retrieve/pii/S1542356514013950

[6] S. Khan, F. Fakhouri, W. Majeed, and A. Kolipaka, "Cardiovascular magnetic resonance elastography: A review," *NMR Biomed.*, vol. 31, no. 10, Oct. 2018, Art. no. e3853. [Online]. Available: https://onlinelibrary.wiley.com/doi/10.1002/nbm.3853

[7] L. V. Hiscox, H. Schwarb, M. D. J. McGarry, and C. L. Johnson, "Aging brain mechanics: Progress and promise of magnetic resonance elastography," *NeuroImage*, vol. 232, May 2021, Art. no. 117889. [Online]. Available: https://linkinghub.elsevier.com/retrieve/pii/S105381192100166X

[8] J. B. Weaver et al., "Brain mechanical property measurement using MRE with intrinsic activation," *Phys. Med. Biol.*, vol. 57, no. 22, pp. 7275–7287, Nov. 2012. [Online]. Available: https://iopscience.iop.org/article/10.1088/0031-9155/57/22/7275

[9] K. Uffmann and M. E. Ladd, "Actuation systems for MR elastography," *IEEE Eng. Med. Biol. Mag.*, vol. 27, no. 3, pp. 28–34, May 2008. [Online]. Available: http://ieeexplore.ieee.org/document/4527219/

[10] R. Muthupillai, D. J. Lomas, P. J. Rossman, J. F. Greenleaf, A. Manduca, and R. L. Ehman, "Magnetic resonance elastography by direct visualization of propagating acoustic strain waves," *Science*, vol. 269, no. 5232, pp. 1854–1857, Sep. 1995. [Online]. Available: https://www.sciencemag.org/lookup/doi/10.1126/science.7569924

[11] R. Sinkus, M. Tanter, T. Xydeas, S. Catheline, J. Bercoff, and M. Fink, "Viscoelastic shear properties of in vivo breast lesions measured by MR elastography," *Magn. Reson. Imag.*, vol. 23, no. 2, pp. 159–165, Feb. 2005. [Online]. Available: https://linkinghub.elsevier.com/retrieve/pii/S0730725X05000391

[12] L. Tan et al., "A numerical framework for interstitial fluid pressure imaging in poroelastic MRE," *PLoS One*, vol. 12, no. 6, Jun. 2017, Art. no. e0178521. [Online]. Available: https://dx.plos.org/10.1371/journal.pone.0178521

[13] D. Fovargue, D. Nordsletten, and R. Sinkus, "Stiffness reconstruction methods for MR elastography," *NMR Biomed.*, vol. 31, no. 10, Oct. 2018, Art. no. e3935. [Online]. Available: https://onlinelibrary.wiley.com/doi/10.1002/nbm.3935

[14] A. Manduca, R. Muthupillai, P. J. Rossman, J. F. Greenleaf, and R. L. Ehman, "Local wavelength estimation for magnetic resonance elastography," in *Proc. 3rd IEEE Int. Conf. Image Process.*, Lausanne, Switzerland, Sep. 1996, pp. 527–530. [Online]. Available: http://ieeexplore.ieee.org/document/560548/

[15] H. Tzschätzsch et al., "Tomoelastography by multifrequency wave number recovery from time-harmonic propagating shear waves," *Med. Image Anal.*, vol. 30, pp. 1–10, May 2016. [Online]. Available: https://linkinghub.elsevier.com/retrieve/pii/S1361841516000025

[16] T. E. Oliphant, A. Manduca, R. L. Ehman, and J. F. Greenleaf, "Complex-valued stiffness reconstruction for magnetic resonance elastography by algebraic inversion of the differential equation," *Magn. Reson. Med.*, vol. 45, no. 2, pp. 299–310, 2001.

[17] S. Avril et al., "Overview of identification methods of mechanical parameters based on full-field measurements," *Experim. Mech.*, vol. 48, no. 4, pp. 381–402, Aug. 2008. [Online]. Available: http://link.springer.com/10.1007/s11340-008-9148-y

[18] A. J. Romano, J. J. Shirron, and J. A. Bucaro, "On the noninvasive determination of material parameters from a knowledge of elastic displacements theory and numerical simulation," *IEEE Trans. Ultrason., Ferroelectr., Freq. Control*, vol. 45, no. 3, pp. 751–759, May 1998.

[19] E. E. W. Van Houten, M. I. Miga, J. B. Weaver, F. E. Kennedy, and K. D. Paulsen, "Three-dimensional subzone-based reconstruction algorithm for MR elastography," *Magn. Reson. Med.*, vol. 45, no. 5, pp. 827–837, May 2001. [Online]. Available: https://onlinelibrary.wiley.com/doi/10.1002/mrm.1111

[20] I. M. Perreard et al., "Effects of frequency- and direction-dependent elastic materials on linearly elastic MRE image reconstructions," *Phys. Med. Biol.*, vol. 55, no. 22, pp. 6801–6815, Nov. 2010. [Online]. Available: https://iopscience.iop.org/article/10.1088/0031-9155/55/22/013

[21] M. D. J. McGarry et al., "Multiresolution MR elastography using nonlinear inversion," *Med. Phys.*, vol. 39, no. 10, pp. 6388–6396, Oct. 2012, doi: 10.1118/1.4754649.

[22] P. R. Perrinez, F. E. Kennedy, E. E. W. Van Houten, J. B. Weaver, and K. D. Paulsen, "Modeling of soft poroelastic tissue in time-harmonic MR elastography," *IEEE Trans. Biomed. Eng.*, vol. 56, no. 3, pp. 598–608, Mar. 2009. [Online]. Available: http://ieeexplore.ieee.org/document/4694123/

[23] M. McGarry et al., "A heterogenous, time harmonic, nearly incompressible transverse isotropic finite element brain simulation platform for MR elastography," *Phys. Med. Biol.*, vol. 66, no. 5, Mar. 2021, Art. no. 055029. [Online]. Available: https://iopscience.iop.org/article/10.1088/1361-6560/ab9a84

[24] D. R. Smith et al., "Anisotropic mechanical properties in the healthy human brain estimated with multi-excitation transversely isotropic MR elastography," *Brain Multiphys.*, vol. 3, Jun. 2022, Art. no. 100051. [Online]. Available: https://linkinghub.elsevier.com/retrieve/pii/S2666522022000089

[25] M. McGarry et al., "Including spatial information in nonlinear inversion MR elastography using soft prior regularization," *IEEE Trans. Med. Imag.*, vol. 32, no. 10, pp. 1901–1909, Oct. 2013. [Online]. Available: http://ieeexplore.ieee.org/document/6542013/

[26] E. E. W. Van Houten, K. D. Paulsen, M. I. Miga, F. E. Kennedy, and J. B. Weaver, "An overlapping subzone technique for MR-based elastic property reconstruction," *Magn. Reson. Med., Off. J. Int. Soc. Magn. Reson. Med.*, vol. 42, no. 4, pp. 779–786, Oct. 1999.

[27] K. D. Paulsen and H. Jiang, "Enhanced frequency-domain optical image reconstruction in tissues through total-variation minimization," *Appl. Opt.*, vol. 35, no. 19, p. 3447, Jul. 1996. [Online]. Available: https://opg.optica.org/abstract.cfm?URI=ao-35-19-3447

[28] A. A. Oberai, N. H. Gokhale, and G. R. O. Feij, "Solution of inverse problems in elasticity imaging using the adjoint method," *Inverse Problems*, vol. 19, no. 2, pp. 297–313, Apr. 2003. [Online]. Available: https://iopscience.iop.org/article/10.1088/0266-5611/19/2/304

[29] L. Tan et al., "Gradient-based optimization for poroelastic and viscoelastic MR elastography," *IEEE Trans. Med. Imag.*, vol. 36, no. 1, pp. 236–250, Jan. 2017. [Online]. Available: http://ieeexplore.ieee.org/document/7556963/

[30] O. Dietrich, J. G. Raya, S. B. Reeder, M. F. Reiser, and S. O. Schoenberg, "Measurement of signal-to-noise ratios in MR images: Influence of multichannel coils, parallel imaging, and reconstruction filters," *J. Magn. Reson. Imag.*, vol. 26, no. 2, pp. 375–385, Aug. 2007. [Online]. Available: https://onlinelibrary.wiley.com/doi/10.1002/jmri.20969

[31] A. J. Hannum, G. McIlvain, D. Sowinski, M. D. J. McGarry, and C. L. Johnson, "Correlated noise in brain magnetic resonance elastography," *Magn. Reson. Med.*, vol. 87, no. 3, pp. 1313–1328, Mar. 2022. [Online]. Available: https://onlinelibrary.wiley.com/doi/10.1002/mrm.29050

[32] E. Van Houten, G. Geymonat, F. Krasucki, and B. Wattrisse, "General guidelines for the performance of viscoelastic property identification in elastography: A Monte–Carlo analysis from a closed-form solution," *Int. J. Numer. Methods Biomed. Eng.*, vol. 39, no. 8, Aug. 2023, Art. no. e3741.

[33] D. T. Seidl, A. A. Oberai, and P. E. Barbone, "The coupled adjoint-state equation in forward and inverse linear elasticity: Incompressible plane stress," *Comput. Methods Appl. Mech. Eng.*, vol. 357, Dec. 2019, Art. no. 112588. [Online]. Available: https://linkinghub.elsevier.com/retrieve/pii/S0045782519304591

[34] W. Aquino and M. Bonnet, "Analysis of the error in constitutive equation approach for time-harmonic elasticity imaging," *SIAM J. Appl. Math.*, vol. 79, no. 3, pp. 822–849, Jan. 2019. [Online]. Available: https://epubs.siam.org/doi/10.1137/18M1231237

[35] S. Ghosh et al., "Modified error in constitutive equations (MECE) approach for ultrasound elastography," *J. Acoust. Soc. Amer.*, vol. 142, no. 4, pp. 2084–2093, Oct. 2017. [Online]. Available: http://asa.scitation.org/doi/10.1121/1.5006911

[36] B. Banerjee, T. F. Walsh, W. Aquino, and M. Bonnet, "Large scale parameter estimation problems in frequency-domain elastodynamics using an error in constitutive equation functional," *Comput. Methods Appl. Mech. Eng.*, vol. 253, pp. 60–72, Jan. 2013. [Online]. Available: https://linkinghub.elsevier.com/retrieve/pii/S0045782512002770

[37] M. I. Diaz, W. Aquino, and M. Bonnet, "A modified error in constitutive equation approach for frequency-domain viscoelasticity imaging using interior data," *Comput. Methods Appl. Mech. Eng.*, vol. 296, pp. 129–149, Nov. 2015.

[38] A. T. Anderson et al., "Observation of direction-dependent mechanical properties in the human brain with multi-excitation MR elastography," *J. Mech. Behav. Biomed. Mater.*, vol. 59, pp. 538–546, Jun. 2016.

[39] J. Crutison, M. Sun, and T. J. Royston, "The combined importance of finite dimensions, anisotropy, and pre-stress in acoustoelastography," *J. Acoust. Soc. Amer.*, vol. 151, no. 4, pp. 2403–2413, Apr. 2022.

[40] P. R. Amestoy, I. S. Duff, and J.-Y. L'Excellent, "Multifrontal parallel distributed symmetric and unsymmetric solvers," *Comput. Methods Appl. Mech. Eng.*, vol. 184, nos. 2–4, pp. 501–520, Apr. 2000.

[41] S. Goenezen, P. Barbone, and A. A. Oberai, "Solution of the nonlinear elasticity imaging inverse problem: The incompressible case," *Comput. Methods Appl. Mech. Eng.*, vol. 200, nos. 13–16, pp. 1406–1420, Mar. 2011. [Online]. Available: https://linkinghub.elsevier.com/retrieve/pii/S0045782510003749

[42] C. Guenthner and S. Kozerke, "Encoding and readout strategies in magnetic resonance elastography," *NMR Biomed.*, vol. 31, no. 10, Oct. 2018, Art. no. e3919. [Online]. Available: https://onlinelibrary.wiley.com/doi/10.1002/nbm.3919

[43] M. D. J. McGarry, E. E. W. Van Houten, P. R. Perriñez, A. J. Pattison, J. B. Weaver, and K. D. Paulsen, "An octahedral shear strain-based measure of SNR for 3D MR elastography," *Phys. Med. Biol.*, vol. 56, no. 13, pp. 153–164, Jul. 2011. [Online]. Available: https://iopscience.iop.org/article/10.1088/0031-9155/56/13/N02

[44] A. T. Anderson et al., "Inversion parameters based on convergence and error metrics for nonlinear inversion MR elastography," in *Proc. Intl. Soc. Mag. Reson. Med.*, vol. 25, 2017, p. 1139.

[45] A. A. Oberai, N. H. Gokhale, M. M. Doyley, and J. C. Bamber, "Evaluation of the adjoint equation based algorithm for elasticity imaging," *Phys. Med. Biol.*, vol. 49, no. 13, pp. 2955–2974, Jul. 2004. [Online]. Available: https://iopscience.iop.org/article/10.1088/0031-9155/49/13/013

[46] L. V. Hiscox et al., "Mechanical property alterations across the cerebral cortex due to Alzheimer's disease," *Brain Commun.*, vol. 2, no. 1, Jan. 2020, Art. no. fcz049.

[47] P. V. Bayly and J. R. Garbow, "Pre-clinical MR elastography: Principles, techniques, and applications," *J. Magn. Reson.*, vol. 291, pp. 73–83, Jun. 2018. [Online]. Available: https://linkinghub.elsevier.com/retrieve/pii/S1090780718300168